

Optoelectronic Optimization of Graded-Bandgap Thin-Film AlGaAs Solar Cells

Faiz Ahmad,^{1,*} Akhlesh Lakhtakia,^{1,2} and Peter B. Monk³

¹Pennsylvania State University, Department of Engineering Science and Mechanics,
NanoMM–Nanoengineered Metamaterials Group, University Park, PA 16802, USA

²Danmarks Tekniske Universitet, Institut for Mekanisk Teknologi, Sektion for Konstruktion og
Produktudvikling, DK-2800 Kongens Lyngby, Danmark

³University of Delaware, Department of Mathematical Sciences, 501 Ewing Hall, Newark, DE 19716, USA

*Corresponding author: fua26@psu.edu

Abstract

An optoelectronic optimization was carried out for an $\text{Al}_\xi\text{Ga}_{1-\xi}\text{As}$ (AlGaAs) solar cell containing (i) an n -AlGaAs absorber layer with a graded bandgap and (ii) a periodically corrugated Ag backreflector combined with localized ohmic Pd–Ge–Au backcontacts. The bandgap of the absorber layer was varied either sinusoidally or linearly. An efficiency of 33.1% with the 2000-nm-thick n -AlGaAs absorber layer is predicted with linearly graded bandgap along with silver backreflector and localized ohmic backcontacts, in comparison to 27.4% efficiency obtained with homogeneous bandgap and a continuous ohmic backcontact. Sinusoidal grading of the bandgap is predicted to enhance the maximum efficiency to 34.5%. Thus, grading the bandgap of the absorber layer, along with a periodically corrugated Ag backreflector and localized ohmic Pd–Ge–Au backcontacts can help realize ultrathin and high-efficient AlGaAs solar cells for terrestrial applications.

1 Introduction

Highly efficient and cost-effective solar cells made ecoresponsibly [1] of Earth-abundant materials with low after-use disposal environmental cost are necessary for sustainability [2]. With crystalline-silicon (Si) delivering about 26% efficiency and multicrystalline-Si about 22% efficiency, Si is the photovoltaic material of choice for solar-photovoltaic modules deployed in solar parks and on rooftops [3, 4]. With somewhat higher efficiency and significantly lower weight-to-power ratio [5], gallium arsenide (GaAs) is the current market leader for solar cells deployed for extra-terrestrial applications, but it is prohibitively expensive for terrestrial applications [6].

There are two options to reduce the cost of the GaAs solar cell. The first option is the reduction of the thickness of the GaAs absorber layer [7, 8, 9]. Not only will that option reduce material usage, but it will also enhance manufacturing throughput. However, a thinner absorber layer will reduce the absorption of incident solar photons. Back-surface modifications such as plasmonic nanostructures [10, 8, 11], localized ohmic backcontacts [9], and highly reflective backreflectors [9] have been investigated to tackle the problem of low absorption in ultrathin GaAs solar cells, but enhanced photon trapping does not necessarily translate into higher efficiency [12, 13].

The second option is to grade the bandgap in the absorber layer by adding aluminum (Al) and controlling the compositional ratio of Al to gallium (Ga) [14, 15]. Bandgap grading of the resulting $\text{Al}_\xi\text{Ga}_{1-\xi}\text{As}$ (AlGaAs) absorber layer will allow photon absorption over a wider frequency range. Also, bandgap grading will increase efficiency by creating a drift electric field that will accelerate photogenerated holes towards the p - n junction in the solar cell [14]. Linear bandgap grading has been shown experimentally to increase the open-circuit voltage V_{oc} in AlGaAs solar cells [16], which should assist in enhancing the efficiency η ; however, suboptimal bandgap grading can reduce the short-circuit current density J_{sc} to offset the increase in V_{oc} .

A recent theoretical study on CIGS solar cells shows that V_{oc} can be enhanced while maintaining or even enhancing J_{sc} [13], by optimally grading the bandgap of the absorber layer. Motivated by these results, we combined both options, i.e., thinning [7, 8, 9] and bandgap grading [14, 15, 16] of the absorber layer in a coupled optoelectronic model [17] of a thin-film AlGaAs solar cell. We then used the model to determine optimal geometric and bandgap-grading parameters to maximize η .

The thickness of the AlGaAs absorber layer was allowed to vary from 100 nm to 2000 nm, and the bandgap was allowed to vary either linearly or sinusoidally along the thickness direction. In addition, we incorporated a highly reflective periodically corrugated silver (Ag) backreflector and *localized* ohmic

backcontacts of palladium (Pd), germanium (Ge), and gold (Au) trilayers [9], with the areal ratio $\zeta \in [0, 1]$ of Pd–Ge–Au and Ag being a geometric parameter for optimization. When $\zeta = 1$, the Ag backreflector is absent while a Pd–Ge–Au trilayer extends across the entire back surface as is typical for a GaAs solar cell [18, 7].

The coupled optoelectronic model has an optical part and an electrical part. In the optical part, the rigorous coupled-wave approach (RCWA) [19, 20] is used to determine the electron–hole–pair generation rate in the semiconductor layers of the solar cell [17, 13], assuming normal illumination by unpolarized polychromatic light endowed with the AM1.5G solar spectrum [21]. In the electrical part, the electron–hole–pair generation rate is used as an input to the one-dimensional (1D) drift-diffusion equations [22, 23] applied to the semiconductor layers. These equations are solved using a hybridizable discontinuous Galerkin (HDG) scheme [24, 25, 26, 27, 28] to determine the current density J_{dev} and the electrical power density $P = J_{\text{dev}}V_{\text{ext}}$ as functions of the bias voltage V_{ext} under steady-state conditions. In turn, the $J_{\text{dev}}-V_{\text{ext}}$ and the $P-V_{\text{ext}}$ curves yield J_{sc} , V_{oc} , and η . Finally, the differential evolution algorithm (DEA) [29] is used to maximize η as a function of various geometric and bandgap-grading parameters.

The structure of this paper is as follows. Section 2 contains the optical and the electrical descriptions of the AlGaAs solar cell. As implementation details for the optical [12, 17] and the electronic parts [17, 13] of the model as well as the DEA [30, 31] for solar-cell problems have been published, we have not provided them in this paper. Section 3 divided into four subsections. The efficiency of the solar cell with a 2000-nm-thick GaAs layer as predicted by the model is compared with experimental results [18] in Sec. 3.3.1.1. The effects of the periodically corrugated Ag backreflector along with localized ohmic Pd–Ge–Au backcontacts on the performance of the GaAs solar cells are discussed in Sec. 3.3.1.2. Next, optimal results for solar cells with a homogeneous AlGaAs absorber layer (Sec 3.3.2), an AlGaAs absorber layer with linearly graded bandgap (Sec. 3.3.3), and an AlGaAs absorber layer with sinusoidally graded bandgap (Sec. 3.3.4) are provided, each solar cell possessing a periodically corrugated Ag backreflector along with localized ohmic Pd–Ge–Au backcontacts. The paper concludes with some remarks in Sec. 4.

2 Optical and Electrical Descriptions

The solar cell occupies the region $\mathcal{X} : \{(x, y, z) | -\infty < x < \infty, -\infty < y < \infty, 0 < z < L_t\}$, with the half spaces $z < 0$ and $z > L_t$ occupied by air. The reference unit cell, identified as $\mathcal{R} : \{(x, y, z) | -L_x/2 < x < L_x/2, -\infty < y < \infty\}$, is schematically depicted in Fig. 1.

The region $0 < z < L_{\text{MgF}_2} = 110$ nm is occupied by magnesium fluoride (MgF_2) [32] and the region $L_{\text{MgF}_2} < z < L_{\text{ARC}} = 150$ nm by zinc sulfide (ZnS) [33], the two layers collectively functioning to reduce light reflection [18]. The region $L_{\text{ARC}} < z < L_{\text{ARC}} + L_{\text{FSP}}$ is a 20-nm-thick front-surface passivation (FSP) layer of $p^+-\text{Al}_{0.51}\text{In}_{0.49}\text{P}$ (hereafter referred as AlInP) [34] to reduce the front-surface recombination rate and thereby improve J_{sc} [35]. Next, homogeneous $p\text{-Al}_{\xi}\text{Ga}_{1-\xi}\text{As}$ [36] with fixed ξ occupies the 50-nm-thick region $L_{\text{ARC}} + L_{\text{FSP}} < z < L_{\text{ARC}} + L_{\text{FSP}} + L_w$ to form a $p\text{-}n$ junction with an $n\text{-Al}_{\xi}\text{Ga}_{1-\xi}\text{As}$ [36] absorber layer of thickness $L_s \in [100, 2200]$ nm. The quantity ξ is taken to be dependent on z in this paper. With $L_d = L_{\text{ARC}} + L_{\text{FSP}} + L_w + L_s + L_{\text{BSP}}$, the region $L_d - L_{\text{BSP}} < z < L_d$ of thickness $L_{\text{BSP}} = 20$ nm is a back-surface passivation (BSP) layer of $n^+\text{-Ga}_{0.49}\text{In}_{0.51}\text{P}$ (hereafter referred as GaInP) [37] to reduce the back-surface recombination rate and thereby improve J_{sc} [35, 38].

The region $L_d < z < L_d + L_m$ in \mathcal{R} has a complicated morphology. A Pd–Ge–Au triple layer of width ζL_x , $\zeta \in (0, 1)$, along the x axis serves as the localized ohmic back contact [9] comprising a Pd layer of thickness $L_{\text{Pd}} = 20$ nm [39], a Ge layer of thickness $L_{\text{Ge}} = 50$ nm [40], and an Au layer of thickness $L_{\text{Au}} = 100$ nm [39]. The remainder of the region $L_d < z < L_d + L_m$ is occupied by Ag [39] for optical reflection. Finally, the region $L_d + L_m < z < L_d + L_m + L_{\text{Ag}} = L_t$, $L_{\text{Ag}} = 100$ nm, is occupied by Ag serving as an optical backreflector.

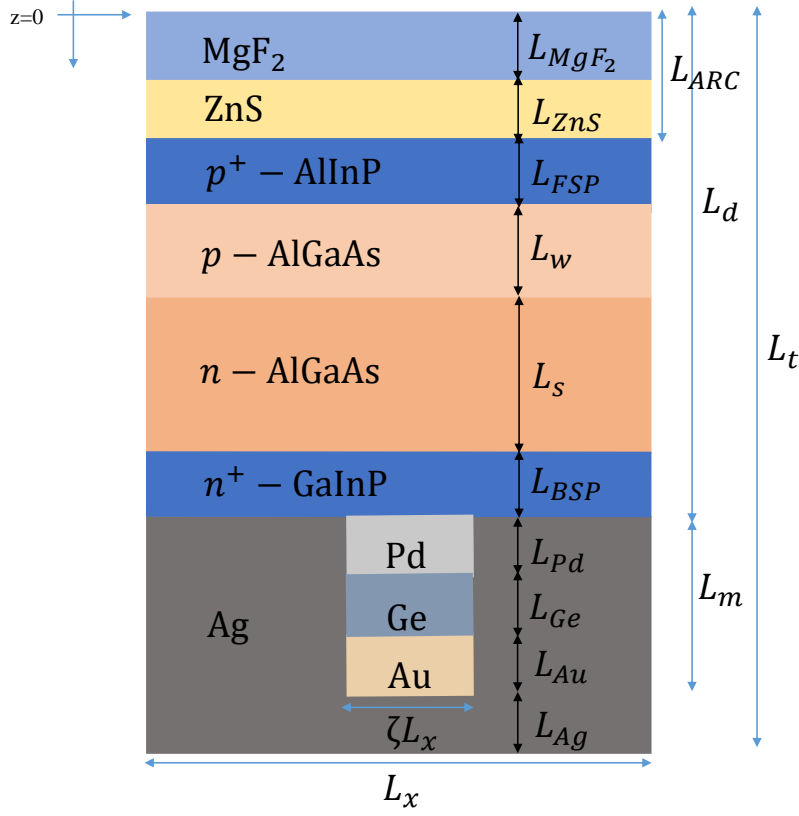


Figure 1: Schematic of the reference unit cell \mathcal{R} of the AlGaAs solar cell.

The linear variation of bandgap in the n -AlGaAs absorber layer was modeled as [12, 13]

$$\begin{aligned}
 E_g(z) &= E_{g,\min} \\
 &+ A(E_{g,\max} - E_{g,\min}) \frac{z - (L_{\text{ARC}} + L_{\text{FSP}} + L_w)}{L_s}, \\
 z &\in [L_{\text{ARC}} + L_{\text{FSP}} + L_w, L_{\text{ARC}} + L_{\text{FSP}} + L_w + L_s],
 \end{aligned} \tag{1}$$

where $E_{g,\min}$ is the minimum bandgap, $E_{g,\max}$ is the maximum bandgap, and A is an amplitude (with $A = 0$ representing a homogeneous AlGaAs layer). The bandgap is thus minimum at the front face $z = L_{\text{ARC}} + L_{\text{FSP}} + L_w$ and maximum at the back face $z = L_{\text{ARC}} + L_{\text{FSP}} + L_w + L_s$ of the absorber layer. The reverse grading (i.e., maximum at $z = L_{\text{ARC}} + L_{\text{FSP}} + L_w$ and minimum at $z = L_{\text{ARC}} + L_{\text{FSP}} + L_w + L_s$) did not give satisfactory results.

The sinusoidal variation of the bandgap in the n -AlGaAs absorber layer was modeled as [12, 13, 41]

$$\begin{aligned}
 E_g(z) &= E_{g,\min} + A(E_{g,\max} - E_{g,\min}) \\
 &\times \left\{ \frac{1}{2} \left[\sin \left(2\pi K \frac{z - (L_{\text{ARC}} + L_{\text{FSP}} + L_w)}{L_s} - 2\pi\psi \right) + 1 \right] \right\}^\alpha, \\
 z &\in [L_{\text{ARC}} + L_{\text{FSP}} + L_w, L_{\text{ARC}} + L_{\text{FSP}} + L_w + L_s],
 \end{aligned} \tag{2}$$

where $\psi \in [0, 1]$ describes a relative phase shift, K is the number of periods in the AlGaAs layer, and $\alpha > 0$ is a shaping parameter. The parameter $\bar{\xi}$ for the homogeneous p -AlGaAs layer governs the bandgap $E_{g,w}$ in

that layer. Optical spectra of the relative permittivities of all materials used in the solar cell are provided in Appendix A.

The RCWA [19, 20] was used to calculate the electric field phasor $\underline{E}(x, z, \lambda_0)$ everywhere inside the solar cell as a result of illumination by a monochromatic plane wave normally incident on the plane $z = 0$ from the half space $z < 0$, λ_0 being the free-space wavelength. The electric field phasor of the incident plane wave was taken as $\underline{E}_{\text{inc}}(z, \lambda_0) = E_0 \frac{\hat{u}_x + \hat{u}_y}{\sqrt{2}} \exp(ik_0 z)$ with $E_0 = 4\sqrt{15\pi} \text{ V m}^{-1}$. With the assumption that every absorbed photon excites an electron-hole pair, the x -averaged electron-hole-pair generation rate was calculated as [13]

$$G(z) = \frac{\eta_0}{\hbar E_0^2} \frac{1}{L_x} \int_{-L_x/2}^{L_x/2} \left[\int_{\lambda_{0,\min}}^{\lambda_{0,\max}} \text{Im}\{\varepsilon(x, z, \lambda_0)\} |\underline{E}(x, z, \lambda_0)|^2 \times S(\lambda_0) d\lambda_0 \right] dx \quad (3)$$

for $z \in [L_{\text{ARC}}, L_d]$, where \hbar is the reduced Planck constant, $\eta_0 = 120\pi \Omega$ is the intrinsic impedance of free space, $S(\lambda_0)$ is the AM1.5G solar spectrum [21], $\lambda_{0,\min} = 300 \text{ nm}$, and $\lambda_{0,\max} = (1240/E_{g,\min}) \text{ nm}$ with $E_{g,\min}$ in eV. For use in the electrical part of the model, $G(z)$ contains the effects of highly reflective Ag, the localized ohmic Pd-Ge-Au backcontacts, and the MgF_2/ZnS double-layer antireflection coating. The x -averaging is justified since the charge carriers generally flow along the z axis because the solar cell operates under the influence of a bias voltage V_{ext} applied along the same axis; furthermore, $L_x \sim 500 \text{ nm}$ is minuscule in comparison to the lateral dimensions of the solar cell.

The region $L_{\text{ARC}} < z < L_d$ contains four semiconductor layers: the p^+ -AlInP FSP layer, the p -AlGaAs layer, the n -AlGaAs absorber layer, and the n^+ -GaInP BSP layer. All four were incorporated in the electrical part [13, 17] of the model, as all four contribute to charge-carrier generation. Electrical parameters used for all four semiconductor layers [42, 43, 44, 45, 46] are provided in Appendix A.

As the focus here is not on how the solar cell interfaces with an external circuit, both terminals were considered to be ideal ohmic contacts. We used a 1D drift-diffusion model [23, 22, 28] to investigate the transport of electrons and holes. The bandgap-dependent electron affinity $\chi(z)$, the conduction band density of states $N_c(z)$, the valence band density of states $N_v(z)$, the electron mobility $\mu_n(z)$, the hole mobility $\mu_p(z)$, and the DC relative permittivity $\varepsilon_{\text{dc}}(z)$ were incorporated in the electrical calculations. Also, we incorporated all three recombination processes: radiative, Shockley-Read-Hall, and Auger [23, 22]. The Shockley-Read-Hall recombination rate was taken to depend on $E_g(\xi)$ as the trap/defect density N_f , the electron thermal speed $v_{\text{th},n}$, and the hole thermal speed $v_{\text{th},p}$ are ξ dependent in both $\text{Al}_\xi\text{Ga}_{1-\xi}\text{As}$ layers. However, the radiative recombination and Auger recombination rates were considered independent of the bandgap due to lack of available data. The electrical part yields values of J_{sc} , V_{oc} , the fill factor FF [23], and η .

The DEA [29] was used to maximize η with respect to certain geometric and bandgap parameters, using a custom algorithm implemented with MATLAB[®] version R2019a.

3 Numerical results and discussion

3.1 GaAs solar cell

3.1.1 Model validation

First, we validated our coupled optoelectronic model by comparison with the experimental results for the $\text{MgF}_2/\text{ZnS}/\text{AlInP}/p\text{-GaAs}/n\text{-GaAs}/\text{GaInP}/\text{Pd-Ge-Au}$ solar cell containing a $L_s = 2000\text{-nm}$ -thick homogeneous GaAs layer [18]; i.e., without Ag ($L_{\text{Ag}} = 0$ and $\zeta = 1$ in reference to Fig. 1), $\bar{\xi} = 0$, and $\xi(z) \equiv 0 \forall z \in [L_{\text{ARC}} + L_{\text{FSP}} + L_w, L_{\text{ARC}} + L_{\text{FSP}} + L_w + L_s]$.

Values of J_{sc} , V_{oc} , FF , and η obtained from our model are provided in Table 1, as also are the corresponding experimental data [18]. The model predictions are in reasonable agreement with the experimental

data. Furthermore, the model-predicted efficiency of 27.4% is close to the highest efficiency (27.6%) reported [7] for GaAs solar cells, but geometric data is not available in Ref. [7] for a proper comparison with the model predictions.

Parenthetically, no interface defects were taken into consideration in the model, suggesting that all the experimentally observed characteristics can be accounted [43] for by the bulk properties of MgF_2 , ZnS , AlInP , $p\text{-GaAs}$, $n\text{-GaAs}$, GaInP , Pd , Ge , and Au .

Table 1: Comparison of J_{sc} , V_{oc} , FF , and η predicted by the coupled optoelectronic model for a GaAs solar cell with a homogeneous GaAs absorber layer (i.e., $A = 0$) with experimental data [18] for $L_{\text{Ag}} = 0$, $\zeta = 1$, $L_{\text{s}} = 2000$ nm, and $\xi = 0$.

	J_{sc} (mA cm^{-2})	V_{oc} (V)	FF (%)	η (%)
Model	29.8	1.081	85.1	27.4
Experiment [18]	29.5	1.045	84.6	26.1

3.1.2 Effect of *localized* ohmic backcontacts

Typically, the Ag backreflector is absent while a Pd–Ge–Au trilayer extends across the entire back surface of a GaAs solar cell, i.e., $\zeta = 1$ [18, 7]. Therefore, next we considered the effect of the localization of ohmic backcontacts by including Ag for better optical backreflection [9]. We maximized η as a function of $L_{\text{x}} \in [100, 1000]$ nm and $\zeta \in [0.05, 1]$, for $L_{\text{s}} \in \{100, 1000, 2000\}$ nm, $\bar{\xi} = 0$, and $\xi(z) \equiv 0 \forall z \in [L_{\text{ARC}} + L_{\text{FSP}} + L_{\text{w}}, L_{\text{ARC}} + L_{\text{FSP}} + L_{\text{w}} + L_{\text{s}}]$.

For all three values of L_{s} , the efficiency was found to be maximum for $L_{\text{x}} = 510$ nm and $\zeta = 0.05$. Values of J_{sc} , V_{oc} , FF , and η obtained from the coupled optoelectronic model are provided in Table 2. The effect of the inclusion of the Ag backreflector to localize the ohmic Pd–Ge–Au backcontacts is to increase J_{sc} . However, that increase is more for smaller L_{s} . At the same time, V_{oc} decreases significantly for $L_{\text{s}} = 100$ nm, but it does not change for the two higher values of L_{s} . As a result, the efficiency is enhanced from 16.5% to 18.3% (a relative enhancement of 10.9%) for $L_{\text{s}} = 100$ nm, but from 27.4% to just 28.0% (a relative enhancement of 2.1%) for $L_{\text{s}} = 2000$ nm. In other words, the effect of localized ohmic backcontacts on η is significant for thin absorber layers but less pronounced for thick absorber layers.

The value of $\zeta = 0.05$ is in accord with the experimental and theoretical findings of Vandamme *et al.* [9]. Hence, we ensured that $\zeta \geq 0.05$ for optimization of AlGaAs solar cells.

3.2 Optimal AlGaAs solar cell: Homogeneous bandgap

Next, we considered the optoelectronic optimization of the solar cell with a homogeneous $n\text{-AlGaAs}$ absorber layer (i.e., $A = 0$), a periodically corrugated Ag backreflector, and localized ohmic Pd–Ge–Au backcontacts. Whereas $L_{\text{Ag}} = 100$ nm was fixed, the parameter space for optimizing η was chosen as: $E_{\text{g,w}} \in [1.424, 2.09]$ eV, $E_{\text{g,min}} \in [1.424, 2.09]$ eV, $L_{\text{x}} \in [100, 1000]$ nm, and $\zeta \in [0.05, 1]$. The common allowed range of $E_{\text{g,w}}$ and $E_{\text{g,min}}$ is consistent with $\xi \in [0, 0.8]$. Optimization was done for several discrete values of L_{s} ranging from 100 nm to 2000 nm.

Values of J_{sc} , V_{oc} , FF , and η predicted by the coupled optoelectronic model are presented in Table 3 for seven different values of L_{s} . The values of $E_{\text{g,w}}$, $E_{\text{g,min}}$, L_{x} , and ζ for the optimal designs are also provided in the same table.

For the thinnest $n\text{-AlGaAs}$ absorber layer ($L_{\text{s}} = 100$ nm), the maximum efficiency predicted is 18.5% with $E_{\text{g,w}} = 2.09$ eV ($\xi = 0.8$), $E_{\text{g,min}} = 1.424$ eV ($\xi = 0$), and $L_{\text{x}} = 500$ nm. The values of J_{sc} , V_{oc} , and FF

Table 2: J_{sc} , V_{oc} , FF , and η predicted by the coupled optoelectronic model for a GaAs solar cell with a homogeneous GaAs absorber layer (i.e., $A = 0$), when Ag is either absent ($\zeta = 1$) or not ($\zeta < 1$) and $L_s \in \{200, 1000, 2000\}$ nm.

L_s (nm)	L_x (nm)	ζ	L_{Ag} (nm)	J_{sc} (mA cm $^{-2}$)	V_{oc} (V)	FF (%)	η (%)
100	-	1	0	17.3	1.132	84.2	16.5
100	510	0.05	100	19.7	1.093	85.1	18.3
1000	-	1	0	28.3	1.089	85.1	26.3
1000	510	0.05	100	29.4	1.090	85.0	27.3
2000	-	1	0	29.8	1.081	85.1	27.4
2000	510	0.05	100	30.4	1.081	85.1	28.0

corresponding to this optimal design are 18.9 mA cm $^{-2}$, 1.149 V, and 85.1%, respectively. For this design, the n -AlGaAs layer is really a n -GaAs layer but the p -AlGaAs layer is different from a p -GaAs layer. If $\bar{\xi} = 0$ were to be fixed (i.e., the p -AlGaAs layer were to be replaced by a p -GaAs layer, the efficiency would be slightly less at $\sim 18.3\%$ (Table 2).

For the thickest n -AlGaAs absorber layer ($L_s = 2000$ nm), the maximum efficiency predicted is 28.8% with $E_{g,w} = 2.09$ eV ($\bar{\xi} = 0.8$), $E_{g,min} = 1.424$ eV, and $L_x = 500$ nm. The values of J_{sc} , V_{oc} , and FF corresponding to this optimal design are 30.2 mA cm $^{-2}$, 1.090 V, and 87.3%, respectively. Again, for this optimal design, the n -AlGaAs layer is really a n -GaAs layer but the p -AlGaAs layer is different from a p -GaAs layer. If the p -AlGaAs layer were to be replaced by a p -GaAs layer, the efficiency would decrease somewhat to $\sim 28\%$ (Table 2).

Regardless of the value of L_s , the optimal design in Table 3 has $L_x = 505 \pm 5$ nm and $\zeta = 0.05$, similar to the optimal design for its GaAs counterpart (Table 2). Even lower values of ζ would give higher efficiencies but the localized ohmic Pd-Ge-Au backcontacts are necessary because of superior electron-collection capability [9]. Also, both $E_{g,min}$ and $E_{g,w}$ are independent of L_s in Table 3, $E_{g,min}$ being at its minimum allowed value and $E_{g,w}$ at its maximum allowed value.

Table 3: Predicted parameters of the optimal AlGaAs solar cell with a specified value of $L_s \in [100, 2000]$ nm, when the n -AlGaAs absorber layer is homogeneous ($A = 0$), $L_{Ag} = 100$ nm, and $\zeta < 1$.

L_s (nm)	$E_{g,w}$ (eV)	$E_{g,min}$ (eV)	L_x (nm)	ζ	J_{sc} (mA cm $^{-2}$)	V_{oc} (V)	FF (%)	η (%)
100	2.09	1.424	500	0.05	18.9	1.149	85.1	18.5
200	2.09	1.424	510	0.05	21.6	1.128	85.2	20.7
300	2.09	1.424	502	0.05	24.1	1.124	85.7	23.2
400	2.09	1.424	510	0.05	25.8	1.119	86.5	24.9
500	2.09	1.424	500	0.05	27.0	1.117	86.3	26.1
1000	2.09	1.424	500	0.05	29.2	1.104	87.0	28.1
2000	2.09	1.424	510	0.05	30.2	1.090	87.3	28.8

Table 4: Predicted parameters of the optimal AlGaAs solar cell with a specified value of $L_s \in [100, 2000]$ nm, when the n -AlGaAs absorber layer is linearly nonhomogeneous according to Eq. (1), $L_{Ag} = 100$ nm, and $\zeta < 1$.

L_s (nm)	$E_{g,w}$ (eV)	$E_{g,min}$ (eV)	$E_{g,max}$ (eV)	A	L_x (nm)	ζ	J_{sc} (mA cm ⁻²)	V_{oc} (V)	FF (%)	η (%)
100	1.424	1.424	1.98	0.99	500	0.05	16.8	1.399	89.3	21.0
200	1.424	1.424	1.98	0.99	510	0.05	19.0	1.422	81.9	22.2
300	1.424	1.424	1.98	1.0	502	0.05	19.1	1.441	85.3	23.5
400	1.424	1.424	1.98	0.99	510	0.05	19.8	1.453	86.5	24.9
500	1.424	1.424	1.98	0.98	500	0.05	20.5	1.462	87.1	26.1
1000	1.424	1.424	1.98	0.99	500	0.05	22.7	1.486	88.3	29.8
2000	1.424	1.424	1.98	1.0	500	0.05	24.7	1.507	88.8	33.1

3.3 Optimal AlGaAs solar cell: Linearly graded bandgap

3.3.1 Optimal designs

Next, we considered the maximization of η when the bandgap of the n -AlGaAs absorber layer is linearly graded according to Eq. (1), $L_{Ag} = 100$ nm, and $\zeta \neq 1$. The parameter space used for optimizing η was chosen as: $E_{g,w} \in [1.424, 2.09]$ eV, $E_{g,min} \in [1.424, 2.09]$ eV, $E_{g,max} \in [1.424, 2.09]$ eV, $A \in [0, 1]$, $L_x \in [100, 1000]$ nm, and $\zeta \in [0.05, 1]$. The common allowed range of $E_{g,w}$, $E_{g,min}$, and $E_{g,max}$ is consistent with $\xi \in [0, 0.8]$.

Values of J_{sc} , V_{oc} , FF , and η for the optimal designs are presented in Table 4 for seven different values of L_s . The corresponding values of $E_{g,w}$, $E_{g,min}$, $E_{g,max}$, A , L_x , and ζ are also provided in the same table.

For the thinnest n -AlGaAs absorber layer ($L_s = 100$ nm), the maximum efficiency predicted is 21.0% with $E_{g,w} = 1.424$ eV ($\bar{\xi} = 0$), $E_{g,min} = 1.424$ eV ($\xi = 0$), $E_{g,max} = 1.98$ eV ($\xi = 0.45$), $A = 0.99$, and $L_x = 500$ nm. A relative enhancement of 13.5% over the maximum efficiency 18.5% in Table 3 for the homogeneous absorber layer of the same thickness is predicted. The values of J_{sc} , V_{oc} , and FF corresponding to the optimal design are 16.8 mA cm⁻², 1.399 V, and 89.3%, respectively.

For the thickest n -AlGaAs absorber layer ($L_s = 2000$ nm), the maximum efficiency predicted is 33.1% with $E_{g,w} = 1.424$ eV ($\bar{\xi} = 0$), $E_{g,min} = 1.424$ eV ($\xi = 0$), $E_{g,max} = 1.98$ eV ($\xi = 0.45$), $A = 1$, and $L_x = 500$ nm. The values of J_{sc} , V_{oc} , and FF corresponding to this optimal design are 24.7 mA cm⁻², 1.507 V, and 88.8%, respectively. A relative enhancement of 14.9% is predicted with linear bandgap grading of the n -AlGaAs absorber layer over the optimal efficiency of 28.8% with the homogeneous n -AlGaAs absorber layer in Table 3. For this optimal design, the p -AlGaAs layer is really a p -GaAs layer, but the n -AlGaAs absorber layer is different from a n -GaAs absorber layer. Although V_{oc} is significantly higher with the linearly graded bandgap compared to the homogeneous bandgap (Table 3), J_{sc} is lower with the linearly graded bandgap.

Similar to the data for the homogeneous absorber layer provided in Table 3, the optimal designs in Table 4 have $L_x = 505 \pm 5$ nm and $\zeta = 0.05$, regardless of the value of L_s . Also, both $E_{g,min}$ and $E_{g,w}$ are independent of L_s in Table 4, just as in Table 3. For both homogeneous and linearly graded absorber layers, $E_{g,min}$ is at its minimum allowed value; however, the value of $E_{g,w}$ is at its minimum allowed value for the linearly graded absorber layer (Table 4) but at its maximum allowed value for the homogeneous absorber layer (Table 3). The values of $A \sim 1$ and $E_{g,max} = 1.98$ eV are independent of L_s for the linearly graded absorber layer (Table 4), the latter being significantly lower than its maximum allowed value.

3.3.2 Detailed study for highest efficiency

The highest efficiency of 33.1% for the solar cell whose n -AlGaAs absorber layer has a linearly graded bandgap is delivered in Table 4 by the optimal design for $L_s = 2000$ nm. We determined the spatial profiles of the bandgap E_g , electron affinity $\chi(z)$, conduction-band energy $E_c(z)$, valence-band energy $E_v(z)$, intrinsic

energy $E_i(z)$, electron density $n(z)$, hole density $p(z)$, intrinsic charge-carrier density $n_i(z)$, recombination rate $R(z)$, and generation rate $G(z)$ in the absorber layer of this solar cell. Furthermore, we determined the total device current density J_{dev} delivered to an external circuit as well as the electrical power density P as functions of the bias voltage V_{ext} .

Spatial profiles of $E_g(z)$ and $\chi(z)$ for the optimal solar cell with n -AlGaAs absorber layer of thickness $L_s = 2000$ nm are provided in Fig. 2(a), whereas Fig. 3(a) presents the spatial profiles of $E_c(z)$, $E_v(z)$, and $E_i(z)$. The spatial variations of E_c and E_i are similar to that of E_g [Fig. 2(a)]. Figure 3(b) presents the spatial profiles of $n(z)$, $p(z)$, and $n_i(z)$ in steady-state condition. The intrinsic carrier density varies linearly such that it is small where E_g is large and *vice versa*.

Spatial profiles of $G(z)$ and $R(z)$ are given in Fig. 4(a). The generation rate is higher near the front face and lower near the back face of the n -AlGaAs absorber layer, which is in accord [22] with higher electron-hole-pair generation where E_g is lower and *vice versa*. Finally, the $J_{\text{dev}}-V_{\text{ext}}$ characteristics of the solar cell shown in Fig. 4(b) deliver $J_{\text{dev}} = 23.9$ mA cm $^{-2}$ and $V_{\text{ext}} = 1.375$ V for best performance (i.e., for maximum P).

3.4 Optimal AlGaAs solar cell: Sinusoidally graded bandgap

3.4.1 Optimal designs

Finally, we considered the maximization of η when the bandgap of the n -AlGaAs absorber layer is sinusoidally graded according to Eq. (2), $L_{\text{Ag}} = 100$ nm, and $\zeta \neq 1$. The parameter space used for optimizing η was chosen as: $E_{g,w} \in [1.424, 2.09]$ eV, $E_{g,\min} \in [1.424, 2.09]$ eV, $E_{g,\max} \in [1.424, 2.09]$ eV, $A \in [0, 1]$, $\alpha \in [0, 8]$, $K \in [0, 8]$, $\psi \in [0, 1]$, $L_x \in [100, 1000]$ nm, and $\zeta \in [0.05, 1]$.

Values of J_{sc} , V_{oc} , FF , and η predicted by our model presented in Table 5 for seven different values of L_s . The values of $E_{g,w}$, $E_{g,\min}$, $E_{g,\max}$, A , α , K , ψ , L_x , and ζ for the optimal designs are also provided in the same table.

For the thinnest n -AlGaAs absorber layer ($L_s = 100$ nm), the maximum efficiency predicted is 21.2% with $E_{g,w} = 2.09$ eV ($\xi = 0.8$), $E_{g,\min} = 1.424$ eV ($\xi = 0$), $E_{g,\max} = 1.98$ eV ($\xi = 0.45$), $A = 1$, $\alpha = 6$, $K = 3$, $\psi = 0.75$, and $L_x = 510$ nm. The values of J_{sc} , V_{oc} , and FF corresponding to this optimal design are 16.1 mA cm $^{-2}$, 1.455 V, and 90.3%, respectively. A relative enhancement of 14.5% over the optimal efficiency 18.5% for the homogeneous n -AlGaAs absorber layer (Table 3) is predicted.

For the thickest n -AlGaAs absorber layer ($L_s = 2000$ nm), the maximum efficiency predicted is 34.5% with $E_{g,w} = 2.09$ eV ($\xi = 0.8$), $E_{g,\min} = 1.424$ eV ($\xi = 0$), $E_{g,\max} = 1.98$ eV ($\xi = 0.45$), $A = 0.99$, $\alpha = 6$, $K = 3$, $\psi = 0.75$, and $L_x = 550$ nm. The corresponding values of J_{sc} , V_{oc} , and FF are 24.8 mA cm $^{-2}$, 1.556 V, and 89.2%, respectively. A relative enhancement of 19.8% is predicted with sinusoidal grading of n -AlGaAs absorber layer over the optimal efficiency of 28.8% with homogeneous n -AlGaAs absorber layer (Table 3). Just as in Sec. 3.3.3.1, although V_{oc} is significantly higher with the sinusoidally graded bandgap compared to the homogeneous bandgap (Table 3), J_{sc} is lower with the sinusoidally graded bandgap.

The optimal designs in Table 5 have $L_x = 525 \pm 25$ nm and $\zeta = 0.05$. The values of $E_{g,\min}$, $E_{g,\max}$, A , α , and ψ are the same for all values of L_s ; however, $K \in \{1, 2, 3\}$ does vary with L_s . The values of $A \sim 1$ and $E_{g,\max} = 1.98$ eV are independent of L_s for the sinusoidally graded absorber layer (Table 5), the latter being significantly lower than its maximum allowed value.

The highest possible efficiency (34.5%) with a sinusoidally graded n -AlGaAs absorber layer is 4.2% higher than the highest possible efficiency (33.1%) with a linearly graded n -AlGaAs absorber layer (Table 4). The short-circuit current density is almost the same for both linearly and sinusoidal graded n -AlGaAs absorber layers; however, the open-circuit voltage is somewhat higher for sinusoidally graded n -AlGaAs absorber layer. By comparing Tables 4 and 5, we conclude that sinusoidally graded n -AlGaAs absorber layer leads to significantly higher efficiency than the linearly graded n -AlGaAs absorber layer for $L_s \geq 1000$ nm, but both types of graded-bandgap absorber layers deliver practically the same efficiency for $L_s \leq 500$ nm.

Table 5: Predicted parameters of the optimal AlGaAs solar cell with a specified value of $L_s \in [100, 2000]$ nm, when the n -AlGaAs absorber layer is sinusoidally graded according to Eq. (2), $L_{Ag} = 100$ nm, and $\zeta < 1$.

L_s (nm)	$E_{g,w}$ (eV)	$E_{g,min}$ (eV)	$E_{g,max}$ (eV)	A	α	K	ψ	L_x (nm)	ζ	J_{sc} (mA cm ⁻²)	V_{oc} (V)	FF (%)	η (%)
100	2.09	1.424	1.98	1.0	6	3	0.75	510	0.05	16.1	1.455	90.3	21.2
200	2.09	1.424	1.98	1.0	6	1	0.75	520	0.05	19.2	1.471	80.2	22.6
300	2.06	1.424	1.98	1.0	6	1	0.74	512	0.05	19.7	1.486	80.2	23.5
400	2.09	1.424	1.98	1.0	6	1	0.75	509	0.05	20.2	1.497	82.0	24.8
500	2.08	1.424	1.98	1.0	6	1	0.75	524	0.05	20.8	1.505	83.0	26.0
1000	2.09	1.424	1.98	1.0	6	2	0.75	516	0.05	22.5	1.533	87.8	30.4
2000	2.09	1.424	1.98	0.99	6	3	0.75	550	0.05	24.8	1.556	89.2	34.5

3.4.2 Detailed study for highest efficiency

We performed a detailed study for the solar cell with thickest ($L_s = 2000$ nm) sinusoidally graded n -AlGaAs absorber layer, because it delivers the highest efficiency. The variations of E_g and χ with z in the semiconductor region are provided in Fig. 2(b). The magnitude of E_g is large near both faces of the n -AlGaAs absorber layer, which features elevate V_{oc} [13]. The regions in which E_g is small are of substantial thickness, these regions being responsible for elevating $G(z)$ [22].

Figure 5(a) shows the variations of E_c , E_v , and E_i with respect to z . The spatial profiles of E_c and E_i are similar to that of E_g . Figure 5(b) shows the spatial variations of the electron, hole, and intrinsic carrier densities in steady-state condition. The intrinsic carrier density varies sinusoidally such that n_i is small where E_g is large and *vice versa*. Profiles of $G(z)$ and $R(z)$ are shown in Fig. 6(a). The generation rate is higher in regions with lower bandgap and *vice versa*. The J_{dev} - V_{ext} characteristics of the solar cell are shown in Fig. 6(b). Our optoelectronic model predicts $J_{dev} = 23.8$ mA cm⁻² and $V_{ext} = 1.45$ V for best performance.

4 Concluding remarks

A coupled optoelectronic model along with the differential evolution algorithm was implemented to evaluate the effectiveness of grading the bandgap of the n -AlGaAs absorber layer for improving the power conversion efficiency of thin-film AlGaAs solar cells. Both linearly and sinusoidally graded bandgaps were studied, with the semiconductor region of the solar cell backed by a periodically corrugated Ag backreflector combined with the localized ohmic Pd-Ge-Au backcontacts.

A 2000-nm-thick n -AlGaAs absorber layer that is sinusoidally graded can deliver 34.5% efficiency, 24.8 mA cm⁻² short-circuit current density, 1.556 V open-circuit voltage, and 89.2% fill factor. In comparison, the efficiency is 28.8%, the short-circuit current density is 30.2 mA cm⁻², the open-circuit voltage is 1.090 V, and the fill factor is 87.3% when the bandgap of the absorber layer is homogeneous. Efficiency enhancement can also be achieved by linearly grading the bandgap of the n -AlGaAs absorber layer, but the gain is significantly smaller compared to sinusoidal bandgap grading when the absorber layer is at least 1000-nm thick. However, for thinner n -AlGaAs absorber layers, both linearly graded bandgaps and sinusoidally graded bandgaps can provide almost equal efficiency gains over the homogenous bandgap.

When the bandgap is sinusoidally graded in the n -AlGaAs absorber layer, the electron-hole-pair generation rate is higher in the broad small-bandgap regions than elsewhere in the n -AlGaAs absorber layer [22]. The open-circuit voltage is elevated in the optimal designs [13], because the bandgap is high in the vicinity of both faces of the n -AlGaAs absorber layer. Both of these characteristics help to increase the efficiency.

Optoelectronic optimization thus indicates that 34.5% efficiency (Table 5) can be achieved for AlGaAs solar cell with a 2000-nm-thick sinusoidally graded n -AlGaAs absorber layer. This efficiency is significantly higher compared to 27.4% efficiency demonstrated with the homogeneous n -AlGaAs absorber layer with a continuous ohmic Pd–Ge–Au back contact (Table 1). Efficiency improvements of equivalent magnitude—e.g., from 22% to 27.7%—have been predicted by bandgap grading of the CIGS absorber layer in thin-film CIGS solar cells [13]. Thus, bandgap grading can provide a way to realize more efficient thin-film solar cells for ubiquitous harnessing of solar energy at low-wattage levels.

A Optical and electrical parameters

The optical permittivity ε of any material is, in general, a function of λ_0 . The optical relative permittivities of MgF_2 [32], ZnS [33], AlInP [34], GaInP [37], Pd [39], Ge [40], Au [39], and Ag [39] are provided in Fig. 7 for $\lambda_0 \in [300, 950]$ nm. The real and imaginary parts of the optical relative permittivity of AlGaAs are provided in Fig. 8 as functions of $\lambda_0 \in [300, 950]$ nm and $\xi \in [0, 0.8]$ [36], data being unavailable for $\xi \in (0.8, 1]$.

Table 6 provides the values of electrical parameters used for all four semiconductors [42, 43, 44, 45, 46].

Funding. The research of F. Ahmed and A. Lakhtakia was partially supported by US National Science Foundation (NSF) under grant number DMS-1619901. The research of P.B. Monk was partially supported by the US National Science Foundation (NSF) under grant number DMS-1619904.

Acknowledgments. A. Lakhtakia thanks the Charles Godfrey Binder Endowment at the Pennsylvania State University and the Otto Mønsted Foundation for partial support of his research endeavors.

Disclosures. The authors declare no conflicts of interest.

References

- [1] C. Vezzoli and E. Manzini, *Design for Environmental Sustainability* (Springer, 2008).
- [2] P. Hawken (ed.), *Drawdown: The Most Comprehensive Plan Ever Proposed to Reverse Global Warming* (Penguin, 2017).
- [3] M. A. Green, Y. Hishikawa, E. D. Dunlop, D. H. Levi, J. Hohl-Ebinger, and A. W. Y. Ho-Baillie, “Solar cell efficiency tables (version 51),” *Prog. Photovolt.: Res. Appl.* **26**, 3–12 (2018).
- [4] M. A. Green, “Photovoltaic technology and visions for the future,” *Prog. Energy* **1**, 013001 (2019).
- [5] A. van Geelen, P. R. Hageman, G. J. Bauhuis, P. C. van Rijsingen, P. Schmidt, and L. J. Giling, “Epitaxial lift-off GaAs solar cell from a reusable GaAs substrate,” *Mater. Sci. Eng. B* **45**, 162–171 (1997).
- [6] K. A. W. Horowitz, T. Remo, B. Smith, and A. Ptak, Techno-Economic Analysis and Cost Reduction Roadmap for III-V Solar Cells (NREL/TP-6A20-72103, 2018) (accessed 08 October 2019).
- [7] B. M. Kayes, H. Nie, R. Twist, S. G. Spruytte, F. Reinhardt, I. C. Kizilyalli, and G. S. Hgashi, “27.6% conversion efficiency, a new record for single-junction solar cells under 1 sun illumination,” *Proc. 37th IEEE Photovolt. Special. Conf. (PVSC)*, Seattle, WA, USA, 19–24 June (2011).
- [8] S.-M. Lee, A. Kwong, D. Jung, J. Faucher, R. Biswas, L. Shen, D. Kang, M. L. Lee, and J. Yoon, “High performance ultrathin GaAs solar cells enabled with heterogeneously integrated dielectric periodic nanostructures,” *ACS Nano* **9**, 10356–10365 (2015).
- [9] N. Vandamme, H.-L. Chen, A. Gaucher, B. Behaghel, A. Lemaître, A. Cattoni, C. Dupuis, N. Bardou, J. F. Guillemoles, and S. Collin, “Ultrathin GaAs solar cells with a silver back mirror,” *IEEE J. Photovolt.* **5**, 565–570 (2015).

- [10] J. Xiao, H. Fang, R. Su, K. Li, J. Song, T. F. Krauss, J. Li, and E. R. Martins, “Paths to light trapping in thin film GaAs solar cells,” *Opt. Express* **26**, A341–A351 (2018).
- [11] W. Yang, J. Becker, S. Liu, Y.-S. Kuo, J.-J. Li, B. Landini, K. Campman, and Y.-H. Zhang, “Ultra-thin GaAs single-junction solar cells integrated with a reflective back scattering layer,” *J. Appl. Phys.* **115**, 203105 (2014).
- [12] F. Ahmad, T. H. Anderson, P. B. Monk, and A. Lakhtakia, “Optimization of light trapping in ultrathin nonhomogeneous $\text{CuIn}_{1-\xi}\text{Ga}_\xi\text{Se}_2$ solar cell backed by 1D periodically corrugated backreflector,” *Proc. SPIE* **10731**, 107310L (2018).
- [13] F. Ahmad, T. H. Anderson, P. B. Monk, and A. Lakhtakia, “Efficiency enhancement of ultrathin CIGS solar cells by optimal bandgap grading,” *Appl. Opt.* **58**, 6067–6078 (2019).
- [14] J. A. Hutchby, “High-efficiency graded band-gap $\text{Al}_x\text{Ga}_{1-x}\text{As}$ -GaAs solar cell,” *Appl. Phys. Lett.* **26**, 457–459 (1975).
- [15] I. M. Dharmadasa, “Third generation multi-layer tandem solar cells for achieving high conversion efficiencies,” *Sol. Energy Mater. Sol. Cells* **85**, 293–300 (2005).
- [16] I. M. Dharmadasa, A. A. Ojo, H. I. Salim, and R. Dharmadasa, “Next generation solar cells based on graded bandgap device structures utilising rod-type nano-materials,” *Energies* **8**, 5440–5458 (2015).
- [17] T. H. Anderson, B. J. Civiletti, P. B. Monk, and A. Lakhtakia, “Coupled optoelectronic simulation and optimization of thin-film photovoltaic solar cells,” *J. Comput. Phys.* **407**, 109242 (2020).
- [18] G. Bauhuis, P. Mulder, E. J. Haverkamp, J. C. C. M. Huijben, and J. J. Schermer, “26.1% thin-film GaAs solar cell using epitaxial lift-off,” *Solar Energ. Mater. Solar Cells* **93**, 1488–1491 (2009).
- [19] E. N. Glytsis and T. K. Gaylord, “Rigorous three-dimensional coupled-wave diffraction analysis of single and cascaded anisotropic gratings,” *J. Opt. Soc. Am. A* **4**, 2061–2080 (1987).
- [20] J. A. Polo, Jr., T. G. Mackay, and A. Lakhtakia, *Electromagnetic Surface Waves: A Modern Perspective* (Elsevier, 2013).
- [21] National Renewable Energy Laboratory, Reference Solar Spectral Irradiance: Air Mass 1.5 (accessed 27 August 2019).
- [22] S. J. Fonash, *Solar Cell Device Physics* (Academic Press, 2010).
- [23] J. Nelson, *The Physics of Solar Cells* (Imperial College Press, 2003).
- [24] C. Lehrenfeld, *Hybrid Discontinuous Galerkin Methods for Solving Incompressible Flow Problems*, Diplomingenieur Thesis, Rheinisch-Westfälischen Technischen Hochschule, Aachen, Germany (2010).
- [25] B. Cockburn, J. Gopalakrishnan, and R. Lazarov, “Unified hybridization of discontinuous Galerkin, mixed, and continuous Galerkin methods for second order elliptic problems,” *SIAM J. Numer. Anal.* **47**, 1319–1365 (2009).
- [26] G. Fu, W. Qiu, and W. Zhang, “An analysis of HDG methods for convection-dominated diffusion problems,” *ESAIM: Math. Model. Numer. Anal.* **49**, 225–256 (2015).
- [27] D. Brinkman, K. Fellner, P. Markowich, and M.-T. Wolfram, “A drift-diffusion-reaction model for excitonic photovoltaic bilayers: Asymptotic analysis and a 2-D HDG finite-element scheme,” *Math. Models Methods Appl. Sci.* **23**, 839–872 (2013).
- [28] F. Brezzi, L. D. Marini, S. Micheletti, P. Pietra, R. Sacco, and S. Wang, “Discretization of semiconductor device problems (I),” In: W. H. A. Schilders and E. J. W. ter Maten (eds), *Handbook of Numerical Analysis: Numerical Methods for Electrodynamical Problems*, pp. 317–342 (Elsevier, 2005).

- [29] R. Storn and K. Price, “Differential evolution—a simple and efficient heuristic for global optimization over continuous spaces,” *J. Global Optim.* **11**, 341–359 (1997).
- [30] M. Solano, M. Faryad, A. S. Hall, T. E. Mallouk, P. B. Monk, and A. Lakhtakia, “Optimization of the absorption efficiency of an amorphous-silicon thin-film tandem solar cell backed by a metallic surface-relief grating,” *Appl. Opt.* **52**, 966–979 (2013).
- [31] M. Solano, M. Faryad, A. S. Hall, T. E. Mallouk, P. B. Monk, and A. Lakhtakia, “Optimization of the absorption efficiency of an amorphous-silicon thin-film tandem solar cell backed by a metallic surface-relief grating: erratum,” *Appl. Opt.* **54**, 398–399 (2015).
- [32] M. J. Dodge, “Refractive properties of magnesium fluoride,” *Appl. Opt.* **23**, 1980–1985 (1984).
- [33] M. R. Querry, *Optical Constants of Minerals and Other Materials from the Millimeter to the Ultraviolet* (CRDEC-CR-88009, 1987) (accessed 08 July 2019).
- [34] E. Ochoa-Martínez, L. Barrutia, M. Ochoa, E. Barrigón, I. García, I. Rey-Stolle, C. Algora, P. Basa, G. Kronome, and M. Gabás, “Refractive indexes and extinction coefficients of n- and p-type doped GaInP, AlInP and AlGaInP for multijunction solar cells,” *Sol. Energy Mater. Sol. Cells* **174**, 388–396 (2018).
- [35] S. R. Kurtz, J. M. Olson, D. J. Friedman, J. F. Geisz, K. A. Bertness, and A. E. Kibbler, “Passivation of interfaces in high-efficiency photovoltaic devices,” *MRS Symp. Proc.* **573**, 95–106 (1999).
- [36] D. E. Aspnes, S. M. Kelso, R. A. Logan, and R. Bhat, “Optical properties of $\text{Al}_x\text{Ga}_{1-x}\text{As}$,” *J. Appl. Phys.* **60**, 754–767 (1986).
- [37] M. Schubert, V. Gottschalch, C. M. Herzinger, H. Yao, P. G. Snyder, and J. A. Woollam, “Optical constants of $\text{Ga}_x\text{In}_{1-x}\text{P}$ lattice matched to GaAs,” *J. Appl. Phys.* **77**, 3416–3419 (1995).
- [38] O. von Roos, “A simple theory of back surface field (BSF) solar cells,” *J. Appl. Phys.* **49**, 3503–3511 (1978).
- [39] P. B. Johnson and R. W. Christy, “Optical constants of the noble metals,” *Phys. Rev. B* **6**, 4370–4379 (1972).
- [40] G. E. Jellison Jr., “Optical functions of GaAs, GaP, and Ge determined by two-channel polarization modulation ellipsometry,” *Opt. Mater.* **1**, 151–160 (1992).
- [41] T. H. Anderson, A. Lakhtakia, and P. B. Monk, “Optimization of nonhomogeneous indium-gallium-nitride Schottky-barrier thin-film solar cells,” *J. Photon. Energy* **8**, 034501 (2018).
- [42] I. Vurgaftman, J. R. Meyer, and L. R. Ram-Mohan, “Band parameters for III–V compound semiconductors and their alloys,” *J. Appl. Phys.* **89**, 5815–5875 (2001).
- [43] A. S. Gudovskikh, N. A. Kaluzhniy, V. M. Lantratov, S. A. Mintairov, M. Z. Shvarts, and V. M. Andreev, “Numerical modelling of GaInP solar cells with AlInP and AlGaAs windows,” *Thin Solid Films* **516**, 6739–6743 (2008).
- [44] S. Adachi, “GaAs, AlAs, and $\text{Al}_x\text{Ga}_{1-x}\text{As}$: Material parameters for use in research and device applications,” *J. Appl. Phys.* **58**, R1–R29 (1985).
- [45] S. Adachi (ed), *Properties of Aluminum Gallium Arsenide*, EMIS Datareviews Series No. 7 (INSPEC, Institution of Electrical Engineers, London, UK, 1993).
- [46] Ioffe Institute, $\text{Al}_x\text{Ga}_{1-x}\text{As}$ (accessed 06 October 2019).

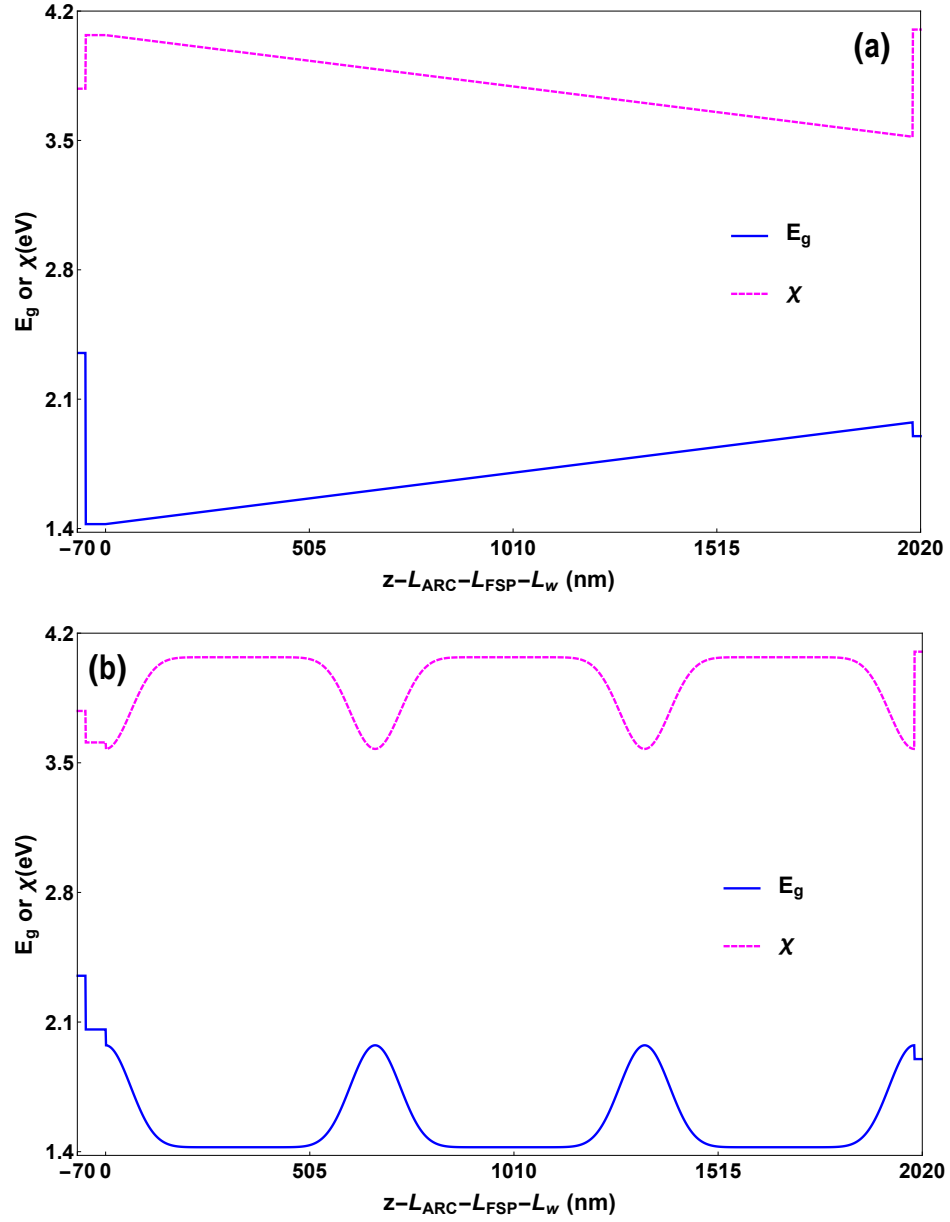


Figure 2: Spatial profiles of $E_g(z)$ and $\chi(z)$ in the four semiconductor layers of the optimal solar cell with the 2000-nm-thick n -AlGaAs absorber layer with (a) linearly graded bandgap and (b) sinusoidally graded bandgap.

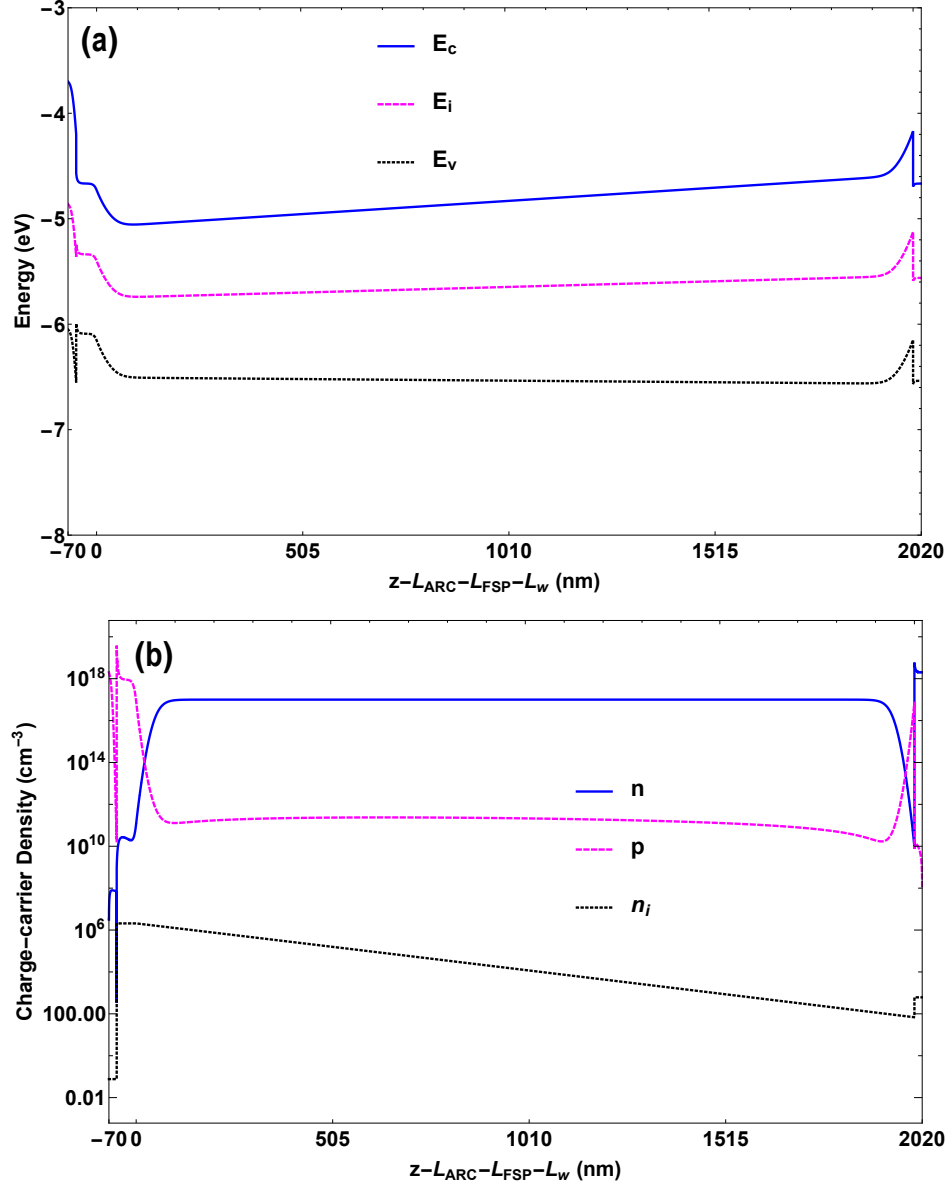


Figure 3: Spatial profiles of (a) $E_c(z)$, $E_v(z)$, and $E_i(z)$, and (b) $n(z)$, $p(z)$, and $n_i(z)$ in the four semiconductor layers of the optimal solar cell with the 2000-nm-thick n -AlGaAs absorber layer with linearly graded bandgap.

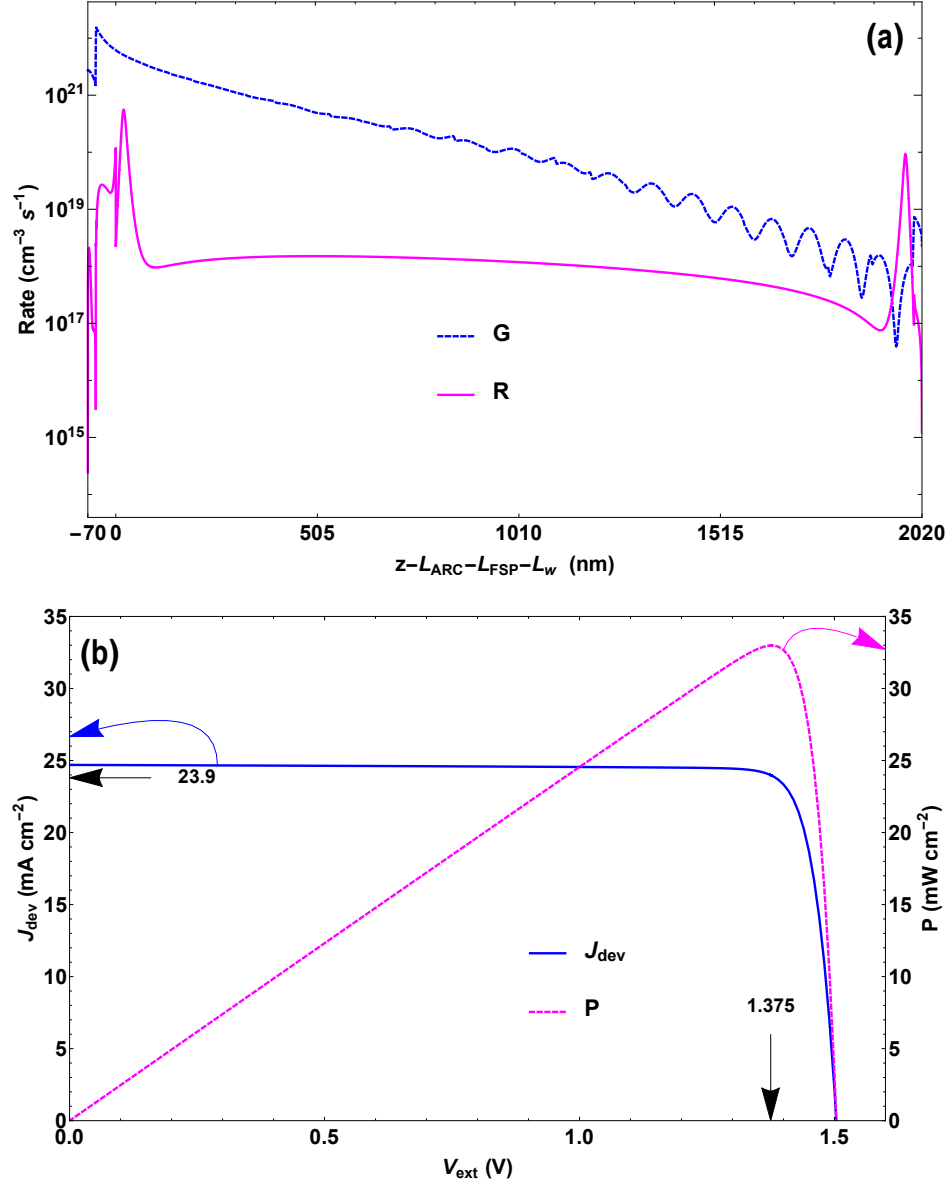


Figure 4: (a) Spatial profiles of $G(z)$ and $R(z)$ in the four semiconductor layers of the optimal solar cell with the 2000-nm-thick n -AlGaAs absorber layer with linearly graded bandgap. (b) $J_{\text{dev}}-V_{\text{ext}}$ and $P-V_{\text{ext}}$ curves of this solar cell. The numerical values of J_{dev} and V_{ext} for maximum P are also identified.

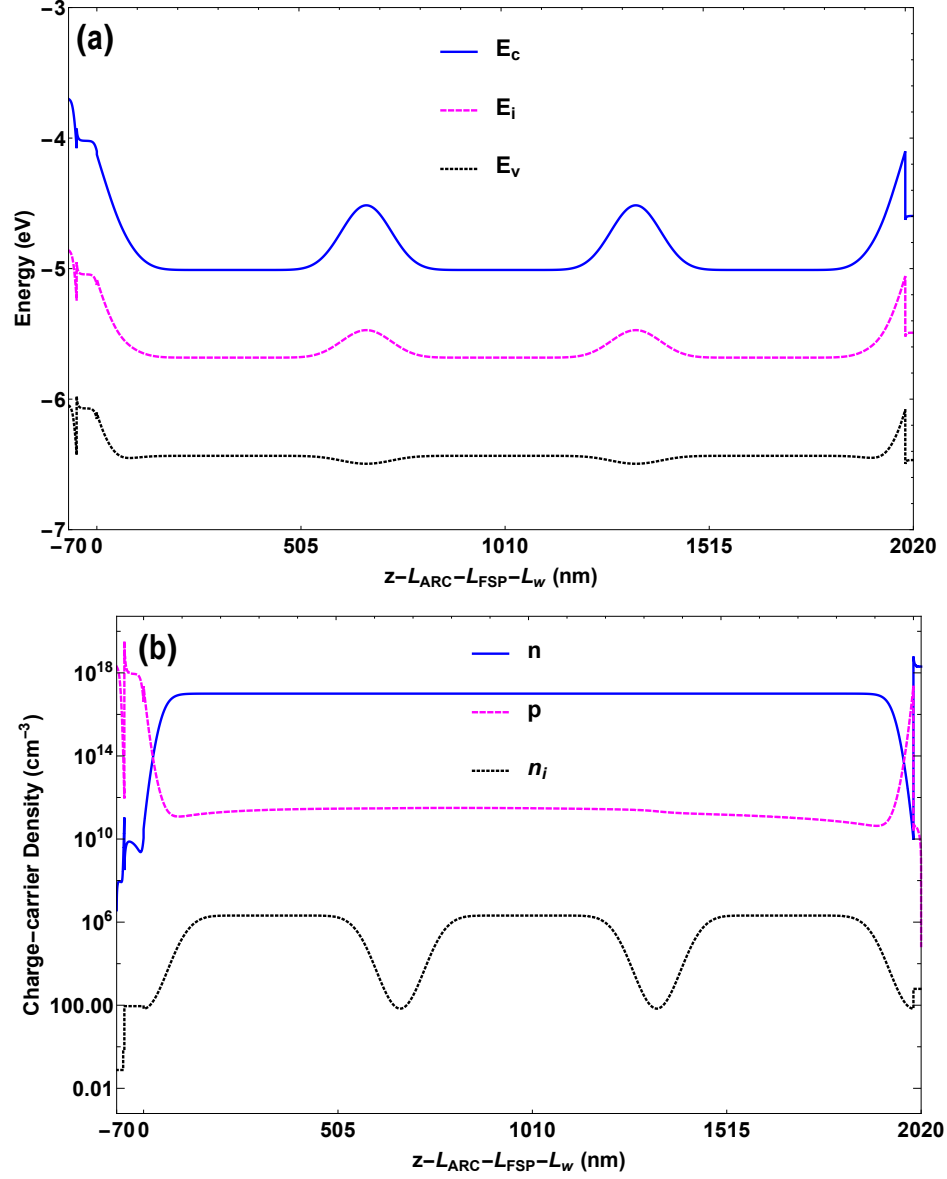


Figure 5: Spatial profiles of (a) $E_c(z)$, $E_v(z)$, and $E_i(z)$, and (b) $n(z)$, $p(z)$, and $n_i(z)$ in the four semiconductor layers of the optimal solar cell with the 2000-nm-thick n -AlGaAs absorber layer with sinusoidally graded bandgap.

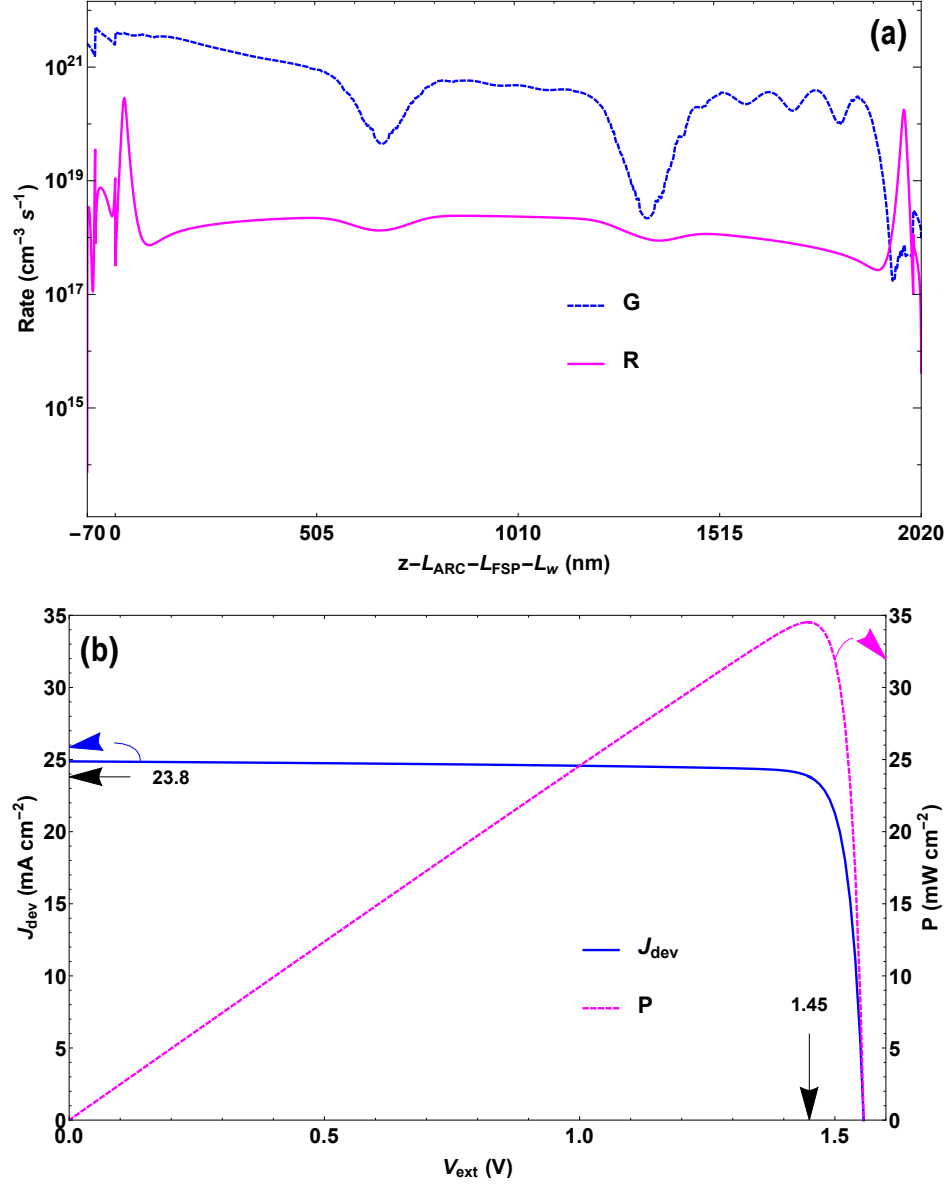


Figure 6: (a) Spatial profiles of $G(z)$ and $R(z)$ in the four semiconductor layers of the optimal solar cell with the 2000-nm-thick n -AlGaAs absorber layer with sinusoidally graded bandgap. (b) $J_{\text{dev}}-V_{\text{ext}}$ and $P-V_{\text{ext}}$ curves of this solar cell. The numerical values of J_{dev} and V_{ext} for maximum P are also identified.

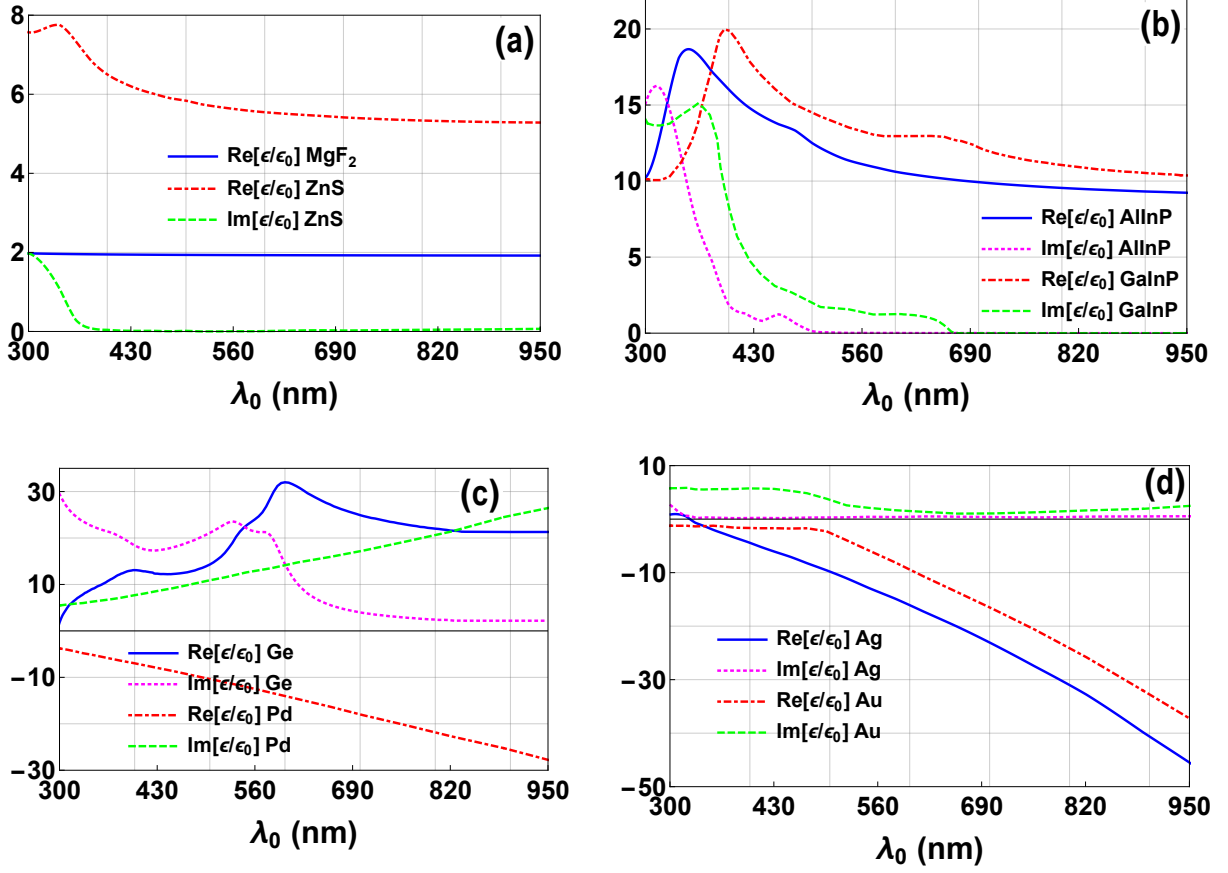


Figure 7: Real and imaginary parts of the optical relative permittivity ϵ/ϵ_0 of (a) MgF_2 , ZnS , (b) AlInP , GaInP , (c) Pd , Ge , (d) Au , and Ag as functions of $\lambda_0 \in [300, 950]$ nm, with ϵ_0 denoting the permittivity of free space. The imaginary part of the relative permittivity of MgF_2 is negligibly small.

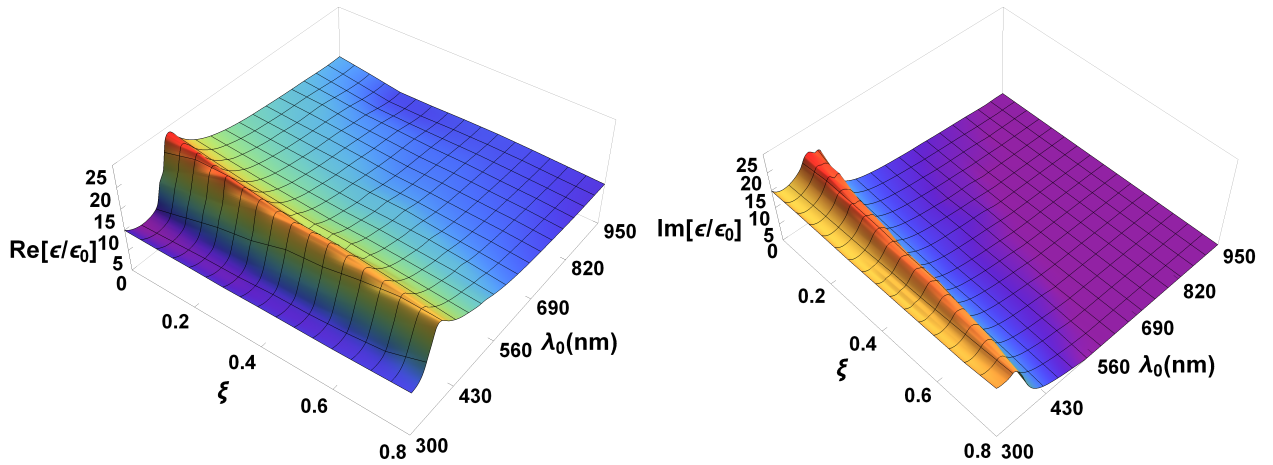


Figure 8: Real and imaginary parts of the optical relative permittivity ϵ/ϵ_0 of AlGaAs as functions of $\lambda_0 \in [300, 950]$ nm and $\xi \in [0, 0.8]$.

Table 6: Electrical properties of AlInP [42, 43], GaInP [46, 42, 43] and $\text{Al}_\xi\text{Ga}_{1-\xi}\text{As}$ [44, 45, 46].

Parameter	Symbol (unit)	AlInP [42, 43]	GaInP [46, 42, 43]	$\text{Al}_\xi\text{Ga}_{1-\xi}\text{As}$ [44, 45, 46]
Bandgap	E_g (eV)	2.35	1.9	$1.424 + 1.247\xi$, $0 \leq \xi < 0.45$; $1.9 + 0.125\xi + 0.143\xi^2$, $0.45 \leq \xi \leq 1$
Electron affinity	χ (eV)	3.78	4.1	$4.07 - 1.1\xi$, $0 \leq \xi < 0.45$; $3.64 - 0.14\xi$, $0.45 \leq \xi \leq 1$
Doping density	N_D (cm^{-3})	2×10^{18} (acceptor)	2×10^{18} (donor)	1×10^{18} (acceptor and donor)
Conduction-band density of states	N_c (cm^{-3})	2.5×10^{18}	6.5×10^{17}	$2.5 \times 10^{19}(0.063 + 0.083\xi)^{3/2}$, $0 \leq \xi < 0.45$; $2.5 \times 10^{19}(0.85 - 0.14\xi)^{3/2}$, $0.45 \leq \xi < 1$
Valence-band density of states	N_v (cm^{-3})	7×10^{18}	1.5×10^{19}	$2.5 \times 10^{19}(0.51 + 0.25\xi)^{3/2}$
Electron mobility	μ_n ($\text{cm}^2\text{V}^{-1}\text{s}^{-1}$)	100	500	$8 \times 10^3 - 2.2 \times 10^4\xi + 10^4\xi^2$, $0 \leq \xi < 0.45$; $-255 + 1160\xi - 720\xi^2$, $0.45 \leq \xi \leq 1$
Hole mobility	μ_p ($\text{cm}^2\text{V}^{-1}\text{s}^{-1}$)	10	30	$370 - 970\xi + 740\xi^2$
DC relative permittivity	ε_{dc}	11.8	11.8	$13.18 - 3.12\xi$
Defect/trap density	N_T (cm^{-3})	10^{17}	10^{17}	$(1 + 9\xi) \times 10^{15}$
Defect/trap level	E_T (eV)	Midgap	Midgap	0.75 eV below conduction-band energy
Electron capture cross section	σ_n (cm^2)	10^{-14}	10^{-14}	10^{-16}
Hole capture cross section	σ_p (cm^2)	10^{-14}	10^{-14}	10^{-16}
Radiative recombination coefficient	R_B ($\text{cm}^3 \text{s}^{-1}$)	10^{-10}	10^{-10}	1.8×10^{-10}
Electron thermal speed	$v_{th,n}$ (cm s^{-1})	10^7	10^7	$(4.4 - 2.1\xi) \times 10^7$
Hole thermal speed	$v_{th,p}$ (cm s^{-1})	10^7	10^7	$(1.8 - 0.5\xi) \times 10^7$
Auger electron recombination coefficient	C_n ($\text{cm}^6 \text{s}^{-1}$)	10^{-30}	10^{-30}	10^{-30}
Auger hole recombination coefficient	C_p ($\text{cm}^6 \text{s}^{-1}$)	10^{-30}	10^{-30}	10^{-30}